Phase stability of BSCF in low oxygen partial pressures

James Ovenstone, Jae-Il Jung, Jeffery S. White, Doreen D. Edwards, Scott T. Misture*

Kazuo Inamori School of Engineering, Alfred University, Alfred, NY 14802, USA

Abstract

In situ X-ray diffraction has been used to investigate the phase stability of barium strontium cobalt iron oxide (BSCF) with the formula $Ba_{0.5}Sr_{0.5}Fe_{1-x}Co_xO_{3-\delta}$ ($x = 0$, 0.2, 0.4, 0.6, 0.8, and 1). The thermal decomposition processes in both low partial pressures of oxygen (air -10^{-5} atm pO_2) and in reducing conditions have been detailed. BSCF manifests excellent stability down to 10^{-5} atm pO_2; however, it decomposes through a complex series of oxides under reducing conditions. Increasing the cobalt content results in a decrease in the temperature range of stability of the material under 4% H_2 in N_2, with the initial decomposition taking place at 375, 425, 550, 600, 650 and 675 °C, for $x = 1$, 0.8, 0.6, 0.4, 0.2 and 0, respectively. Further, the thermal expansion is a strong function of the oxygen activity and Co content. The $x = 0$, 1 end member, BSC, undergoes a phase transition from rhombohedral to cubic symmetry at $\sim$800 °C under 10^{-5} atm pO_2, resulting in an ideal perovskite with $a = 3.9892(3)$ Å at room temperature.
© 2008 Elsevier Inc. All rights reserved.

Keywords: Fuel cell; Cathode; Thermal expansion; Atmosphere; X-ray

1. Introduction

BSCF is a perovskite ceramic, and for fuel cell applications, generally has the formula $Ba_{0.5}Sr_{0.5}Fe_{0.2}Co_{0.8}O_{3-\delta}$. BSCF with this formulation has cubic symmetry, but by changing the ratios of the cations, the structure can adopt rhombohedral symmetry. The material was initially developed as a high-temperature oxygen permeation membrane [1,2], but Shao and Haile demonstrated that ceria fuel cells produced high power densities when using BSCF cathodes [3]. They attributed its excellent performance to the high rate of oxygen diffusion through the material and stated that the rate-limiting step for the process was the oxygen surface exchange. Since the initial paper, numerous studies have been carried out to evaluate BSCF as a cathode material: Duan et al. and Zhu et al. studied the interactions between BSCF and yttria stabilized zirconia (YSZ) and gadolinia doped ceria (GDC), finding that a thin buffer layer of GDC between the YSZ and BSCF improved the stability of the interface and overall performance of the cell [4,5]. Liu et al. fabricated fuel cells using GDC electrolytes and BSCF cathodes and again achieved high power densities when compared to equivalent cells using other cathode materials such as $La_{0.6}Sr_{0.4}Fe_{0.8}Co_{0.2}O_{3-\delta}$ [6]. The performance of BSCF with other electrolyte compositions such as $La_{0.9}Sr_{0.1}Ga_{0.8}Mg_{0.2}O_{2.85}$ [7], and samarium doped ceria carbonate composites has also been investigated with very positive results [8].

A number of groups have tried to improve the performance of BSCF through specialized synthesis techniques to give controlled microstructures, as it is well known that fuel cell performance is greatly dependent on the nature of the interfaces between the various component layers [9–11]. It was found that the synthesis conditions played a significant role in determining the cathode's final performance, thus indicating that significant improvements through novel fabrication techniques should be possible. Other groups have tried to improve further upon the performance of the BSCF by developing composite cathodes such as $Ba_{0.5}Sr_{0.5}Fe_{0.2}Co_{0.8}O_{3-\delta} - Ce_{0.8}Sm_{0.2}O_{1.9}$ and $Ba_{0.5}Sr_{0.5}Fe_{0.2}Co_{0.8}O_{3-\delta} + LaCoO_3$ [12–16]. The composites lower resistance of the cathode, but significant work still needs to be carried out investigating the long-term stabilities of these materials in fuel cell environments.

*Corresponding author. Fax: +1 607 871 2354.

E-mail address: misture@alfred.edu (S.T. Misture).

Yan et al. investigated the effects of CO_2 on the performance of BSCF. Their findings point to a strong absorbance of CO_2 at the surface of the BSCF during cell operation at 500 °C, resulting in the formation of carbonates, which can hinder the electrochemical reduction of oxygen. This effect can be reversed by heating in oxygen at 800 °C [17]. McIntosh et al. [18,19] reported on the oxygen stoichiometry in SCF and the common composition of BSCF, $Ba_{0.5}Sr_{0.5}Fe_{0.2}Co_{0.8}O_{3-\delta}$, in environments with low partial pressure of oxygen (pO_2), and showed that BSCF shows excellent phase stability down to 10^{-5} atm pO_2. In addition, they showed that SCF will undergo an ordering transition to form the vacancy-ordered Brownmillerite structure, but BSCF will not [18]. Lim et al. and Chen et al. both investigated a range of BSCF compositions in which the *B* site cobalt/iron ratio was changed [20,21]. Lim found that the thermal expansion of BSCF increased with increasing cobalt concentration which made higher cobalt material unsuitable for use with scandium stabilized zirconia (ScSZ) electrolytes. Chen found that increasing the iron levels resulted in a decrease in the oxygen permeation flux, and a change in the rate-determining step for permeation from surface exchange to bulk diffusion.

In the current work, we further investigate the phase stability BSCF over the range of Co/Fe ratios in both low pO_2 environments and in the presence of H_2, to establish the fundamentals of phase formation and stability vs. composition. In addition, we investigate the effect of synthesis method on phase stability, comparing commercially available powder prepared through spray pyrolysis, and powders prepared in our laboratory using a modified Pechini method.

2. Experimental methods

Commercial powders were obtained from Praxair Ltd. and used as-received. Laboratory prepared powders were synthesized using a modified Pechini method, using $Ba(NO_3)_2$, $Sr(NO_3)_2$, $Co(NO_3)_2 \cdot 6H_2O$, and $Fe(NO_3)_3 \cdot 9H_2O$ as starting materials. 0.04 mol of ethylenediaminetetraacetic acid (EDTA) was mixed with 40 ml of 1N NH_4OH solution to make NH3-EDTA buffer solution. 0.01 mol of $Ba(NO_3)_2$, 0.01 mol of $Sr(NO_3)_2$, and x(0.02, 0.16, 0.12, 0.08, 0.04, 0) mol of $Co(NO_3)_2 \cdot 6H_2O$ and $(0.02-x)$ mol of $Fe(NO_3)_3 \cdot 9H_2O$, were added to the buffer solution in order to make the required stoichiometries of $Ba_{0.5}Sr_{0.5}Fe_{1-x}Co_xO_{3-\delta}$ ($x = 1.0$, 0.8, 0.6, 0.4, 0.2, and 0.0). 0.06 mol of anhydrous citric acid was added and the pH value was adjusted to 8 by using 1 N NH_4OH solution. Each solution was kept on a hot plate at 100 °C and stirred until gelation took place. After 24 h, the gelled samples were baked in a drying oven at 200 °C for 6 h. The as-produced powders were then calcined at 950 °C for 7 h in air.

High-temperature X-ray diffraction was carried out using a Siemens $\theta-\theta$ D500 diffractometer equipped with a Braun position sensitive detector and custom high-temperature furnace [22] using $CoK\alpha$ radiation with an iron filter. X-ray diffraction data was collected under various controlled atmospheres including air, 4% H_2 with a balance of N_2, and $10^{-5} < pO_2 < 10^{-1}$ atm with a balance of nitrogen. For the oxygen–nitrogen mixtures, gas flows were controlled over the range 1–200 ml/min using two Omega FMA5400/5500 mass flow controllers, and oxygen concentrations were measured using a Thermox CG1000 oxygen analyzer on the outlet side of the diffraction furnace. For air and 4% H_2/balance N_2, gases were supplied from commercially obtained mixtures. The high-temperature experiments, unless otherwise stated, were carried out using a heating rate of 60 °C/min, with measurements made every 25 °C. Measurements were made over the 2θ range 20–130° using a scan rate of 10° 2θ/min. Rietveld analysis was performed using the software PanAlytical HighScore Plus. SEM was carried out using an FEI Quanta 200F field emission environmental SEM equipped with a hot stage, backscatter detector, and EDX detector. A SDT2960 simultaneous DSC-TGA was used for simultaneous TG/DTA experiments using heating rates of 25 °C/min and cooling rates of 15 °C/min.

3. Results and discussion

Fig. 1 shows SEM micrographs of the laboratory prepared $Ba_{0.5}Sr_{0.5}Fe_{1-x}Co_xO_{3-\delta}$ powders. There is a wide particle size range for the powders from around 500 nm up to ~3 μm, with generally uniform morphology.

Fig. 2 shows the refined lattice constants and unit cell volume across the composition range for the laboratory-prepared BSCF samples ($0 < x < 0.8$) in air. In contrast to the work of Lim et al. [20] who showed no diffraction peak shifts with composition, our data clearly shows the expected shift in unit cell size with composition. Samples prepared with $x \leqslant 0.8$ were cubic, whereas the BSC end member ($x = 1.0$) was rhombohedral. As the cobalt concentration increases, we see an increase in the unit cell volume of the material. Since both Fe^{3+} and Co^{3+} ions have nominally the same ionic radius (0.55 Å), this implies that the Fe ions must be in a higher oxidation state in order to give a smaller unit cell volume. We therefore conclude that the Fe ions are primarily in the 4+ oxidation state, while the Co ions are primarily in the 3+ oxidation state. Furthermore, this result implies that there is a higher oxygen vacancy concentration in the cobalt rich material after cooling, resulting in the slightly non-linear dependence of the unit cell volume. The lattice constants are also summarized in Table 1.

Fig. 3 shows the X-ray diffraction data for the $x = 0.8$ sample heated to 1000 °C in 10^{-5} atm pO_2. Only peaks corresponding to the cubic perovskite structure are noted in the patterns, indicating that the material is stable over the range tested, i.e. 25–1000 °C under $pO_2 = 10^{-5}$ atm.

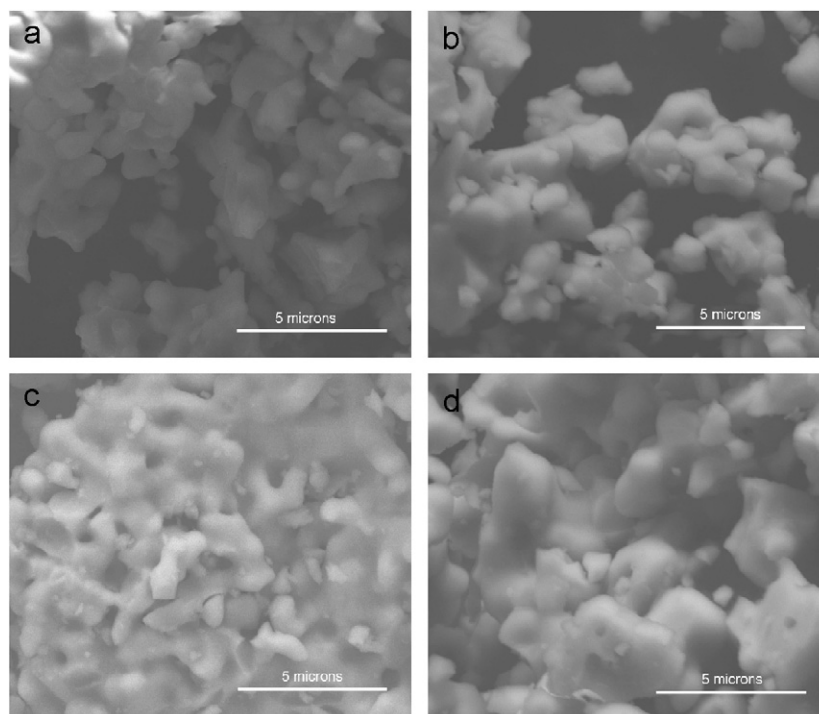The end member BSF ($x = 0$) and all compositions of BSCF, $0.2 \leqslant x \leqslant 0.8$, retained their cubic symmetry upon

Fig. 1. SEM micrographs of laboratory prepared $Ba_{0.5}Sr_{0.5}Fe_{1-x}Co_xO_{3-\delta}$: (a) $x = 0.2$, (b) $x = 0.4$, (c) $x = 0.6$, and (d) $x = 0.8$.
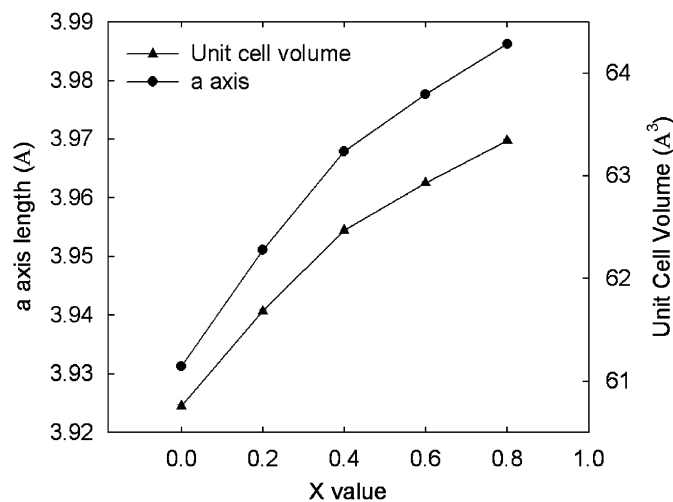
Fig. 2. Unit cell metrics at room temperature for $Ba_{0.5}Sr_{0.5}Fe_{1-x}Co_xO_{3-\delta}$ ($x = 0$–0.8).

heating to 1000 °C with no evidence of decomposition throughout the pO_2 range $10^{-5} < pO_2 < 10^{-1}$ atm. BSCF is significantly more stable than $La_{1-x}Sr_xCoO_{3-\delta}$, which decomposes to form $LaSrCoO_{4-x}$ when heated under $pO_2 = 10^{-5}$ atm [23].

A new phase transition was observed, that of the end member BSC ($x = 1.0$) which manifested a rhombohedral to cubic phase transition at $\sim$800 °C under $pO_2 = 10^{-5}$ atm (see Fig. 4a). The high-temperature cubic phase, which until now has not been reported, was retained upon cooling at 10 °C/min to room temperature (RT). The phase

transition is ascribed to the formation of oxygen ion vacancies during heating in the low pO_2 environment. On cooling to RT, the reverse transition is precluded because of the large proportion of oxygen vacancies that is retained during cooling under reduced oxygen partial pressure. The cubic phase is stable at RT in air since the vacancies are effectively frozen into the structure, however, reheating in air returns the structure to the rhombohedral symmetry.

A Rietveld refinement of the X-ray diffraction data for the cubic high-temperature polymorph of BSC was used to establish the structural details, and is shown in Fig. 4b. Refining the room-temperature dataset demonstrated that the high-temperature polymorph is a cubic perovskite, resulting in refinement statistics $R_{wp} = 6.7\%$ and GOF = 1.2, with the result shown in Fig. 4b. The unit cell details at RT are: $a = 3.9892(3)$ Å, volume = $63.48(2)$ Å^3, and calculated density = $5.74(3)$ g/cm^3.

Fig. 5 shows the unit cell volume expansion, defined as $\Delta V/V_{RT}$, as a function of temperature for BSCF, $0.2 < x < 0.8$ under $pO_2 = 10^{-5}$ atm. The thermal expansion coefficients (slope of the curves) are temperature dependent, but constant thermal expansion coefficients can be obtained over limited temperature ranges (see Table 2). Between 300 and 600 °C, the samples show a marked increase in expansion as a result of equilibration of the oxygen content in the low pO_2 environment, forming a larger fraction of oxygen vacancies. Vacancy formation is accompanied by an anomalously large increase in unit cell volume, or chemical expansion, which is attributed to the reduction of the B-site cations. This behavior is common among other transition-metal defect perovskites, including LSC and LSCF.

Table 1
Lattice constants for laboratory prepared $Ba_{0.5}Sr_{0.5}Fe_{1-x}Co_xO_{3-\delta}$ ($x = 0$–0.8) at room temperature

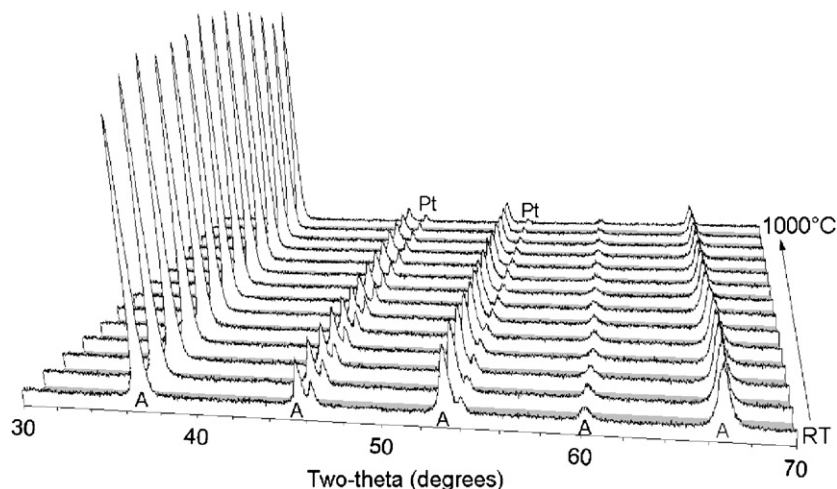| Material	a (Å)	c (Å)	γ (°)	Cell volume (Å^3)	GOF	R_{wp}
$Ba_{0.5}Sr_{0.5}FeO_{3-\delta}$	3.93126(38)	3.93126(38)	90	60.757(18)	1.09	4.99
$Ba_{0.5}Sr_{0.5}Fe_{0.8}Co_{0.2}O_{3-\delta}$	3.95108(34)	3.95108(34)	90	61.681(16)	1.09	4.37
$Ba_{0.5}Sr_{0.5}Fe_{0.6}Co_{0.4}O_{3-\delta}$	3.96783(14)	3.96783(14)	90	62.4680(67)	1.14	4.48
$Ba_{0.5}Sr_{0.5}Fe_{0.4}Co_{0.6}O_{3-\delta}$	3.97758(29)	3.97758(29)	90	62.930(14)	1.12	4.2
$Ba_{0.5}Sr_{0.5}Fe_{0.2}Co_{0.8}O_{3-\delta}$	3.98621(33)	3.98621(33)	90	63.340(16)	1.11	4.13

Fig. 3. *In situ* X-ray diffraction data for laboratory prepared $Ba_{0.5}Sr_{0.5}Fe_{0.2}Co_{0.8}O_{3-\delta}$ heated in 10^{-5} atm pO_2; A = cubic $Ba_{0.5}Sr_{0.5}Fe_{0.2}Co_{0.8}O_{3-\delta}$. Minor diffraction peaks from the Pt sample holder are present. The diffraction patterns were collected in 25 °C steps; however, are shown in 75 °C steps for clarity.

Before quoting values for thermal expansion of BSCF, or, indeed, any related materials, it is critical to define the recent history of the particular specimen in terms of the oxygen pressure, temperature, and cooling rates. For example, Fig. 5 clearly shows the thermal expansion hysteresis for specimens that were annealed at 950 °C in air for 6 h and cooled at 10 K/min, before re-heating under 10^{-5} atm pO_2. When the samples are cooled back to 50 °C, the unit cell volumes return to values larger than observed before heating; a result of a higher concentration of oxygen vacancies. Overall, the total expansion (thermal plus chemical) in these specific specimens increases with increasing iron content, at least during the first heating cycle under low oxygen pressure. Above 500 °C, the samples exhibit thermal expansion coefficients that are nearly independent of temperature and composition, a result in agreement with the recent work of McIntosh et al. [19].

Our first-cycle thermal expansion data is in qualitative agreement with the dilatometry data reported by Zhu et al. [5] who observed an overall increase in thermal expansion with increasing iron content, although they also observed a small decrease from Fe = 0.2 to 0.4. Furthermore, our thermal expansion results at the higher oxygen pressures are in good agreement with the result of McIntosh et al. [19] who studied the $x = 0.2$ composition down to 10^{-3} atm

O$_2$. As shown in Table 2, the trend in our expansion results is reversed on cooling, which is in agreement with the findings of Lim et al. who reported a decrease in thermal expansion coefficient with increasing iron content. It should be noted that the lattice expansions for both the commercial powder (not shown) and the laboratory powders with $x = 0.8$ matched extremely well, indicating that the synthesis method does not significantly affect the expansion. Further experiments on heating BSCF ($x = 0.2$ and 0.8, not shown) demonstrated that the thermal expansion also increases with increasing iron content when heated in air.

Fig. 6 shows the thermogravimetric analysis data collected in air and in 6×10^{-4} atm pO_2 for samples prepared with $x = 0.2$ and 0.8. Samples with $x = 0.4$ and 0.6 were also measured and were qualitatively similar. Upon initial heating in air (Fig. 6a and b) to ~400 °C, the samples did not exhibit any significant weight changes. Continued heating from ~400 to 1000 °C resulted in a steady weight loss, ranging from 0.8% to 2%, as summarized in Table 3. Cooling the samples back to ~400 °C resulted in a steady weight gain. The weight gain (ranging from 0.5% to 1.2%) was generally smaller than the initial weight loss, due to the removal of moisture from the raw powder during initial heating as well as the loss of lattice oxygen. The oxygen vacancy concentration freezes
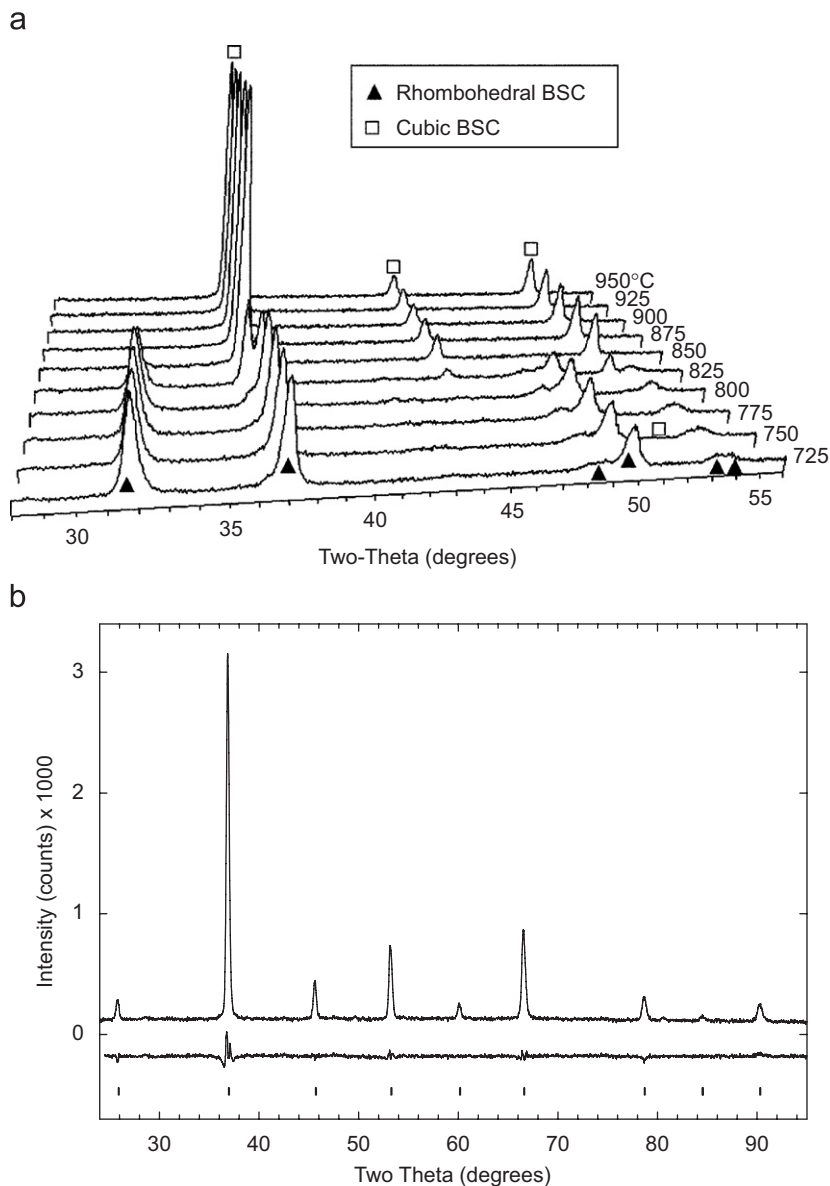
Fig. 4. (a) X-ray diffraction data for laboratory prepared BSC heated in 10^{-5} atm pO_2; A = rhombohedral BSC, and B = cubic BSC. (b) Low-angle region of the XRD data for the cubic phase after Rietveld refinement. Both measured and difference patterns are shown, along with peak position markers.

in at $\sim$400 °C, and further cooling does not result in significant weight changes. After the initial heat up, the TGA curves showed good reproducibility as the powder was thermally cycled, indicating that the powder was able to equilibrate with its surroundings (gaining or losing oxygen) on the time scale of the measurement. After the initial heating cycle, the differences in the weights of the samples at RT and 1000 °C decreased with increasing values of x, suggesting that the level of oxygen ion vacancy generation during heating is smaller as the Co/Fe ratio is increased.

Fig. 6c and d shows the thermal analysis data for the material heated in 6×10^{-4} atm pO_2. The trends are similar to the experiments in air; however, there is a larger difference between the initial heat up weight loss and the

weight gain on cooling. This is due to the raw powder being initially equilibrated in air, and so developing a significantly larger number of oxygen vacancies as it equilibrates to the low oxygen partial pressure during the initial heat up. It is also noteworthy that the weight gains at low pO_2 are smaller than in air, indicating that the materials' oxygen ion vacancy concentration fluctuates with temperature less at low pO_2.

The phase stability was also investigated under reducing conditions, using 4% H_2/balance N_2. Fig. 7 shows the X-ray diffraction patterns of the laboratory prepared BSCF powders as they were heated in 4% H_2/balance N_2, demonstrating that the onset temperature of decomposition increases with increasing iron content. At 1000 °C, all of the samples consisted of a mixture of oxide phases
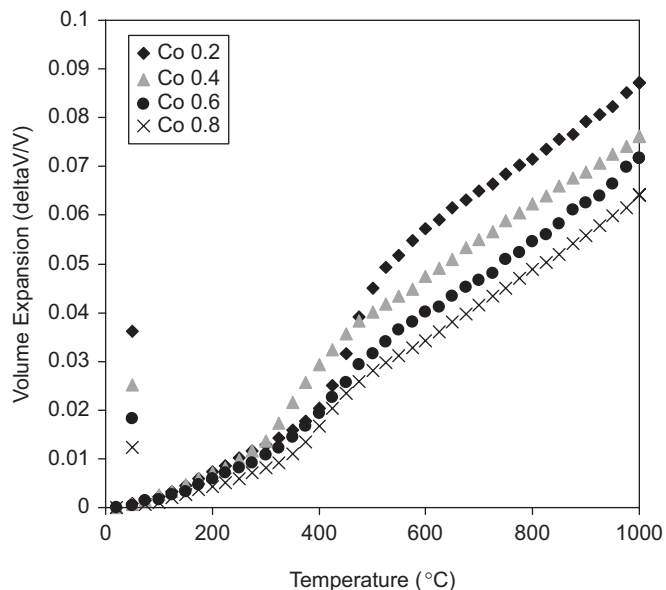
Fig. 5. Lattice expansions for laboratory prepared $Ba_{0.5}Sr_{0.5}Fe_{1-x}Co_xO_{3-\delta}$ heated in 10^{-5} atm pO_2 calculated from X-ray diffraction data. The data points at 50 °C are for the samples after cooling.

Table 2
Equivalent bulk linear thermal expansions calculated from *in situ* X-ray diffraction data for $Ba_{0.5}Sr_{0.5}Fe_{1-x}Co_xO_{3-\delta}$ heated in 10^{-5} atm pO_2

x	600–1000 °C	25–1000 °C	1000–120 °C, cooling
0.2	25.1	29.8	17.3
0.4	23.9	26.0	17.7
0.6	26.4	24.5	18.2
0.8	24.9	22.0	18.4

Units are $10^{-6} K^{-1}$.

and SrO, BaO, and/or a solid solution of the two, and a metal (Co, Fe or a Co/Fe alloy). The products observed at 1000 °C were retained when the samples were cooled to RT. Reheating in air resulted in the reaction of the decomposition products to form the BSCF phases.

The initial decomposition reaction forms Ba_3FeO_5 (or some variant $(Ba,Sr)_3(Co,Fe)O_5$), SrO, and a CoFe alloy of undetermined stoichiometry as major phases. The $(Ba,Sr)_3(Co,Fe)O_5$ decomposes slowly above 575 °C. The SrO decomposes beginning at ∼850 °C, which is accompanied by the growth of (Ba,Sr)O. The solid solution, (Ba,Sr)O, continues to crystallize out to 1000 °C and remains to RT on cooling.

The decomposition reactions differ, however, as the Fe/Co ratio changes in $Ba_{0.5}Sr_{0.5}Fe_{1-x}Co_xO_{3-\delta}$. As the iron content increases, so does the stability range of the BSCF, with initial decompositions taking place at 375, 425, 550, 600, 650 and 675 °C, for $x = 0$, 0.2, 0.4, 0.6, 0.8 and 1, respectively. The end member BSF and the Fe-rich compositions $x = 0.2$, 0.4 and 0.6 decompose to form a phase that matches data in the powder diffraction file

(PDF) for $Ba_6La_2Fe_4O_{15}$. It is important to note that the PDF contains several entries for rare-earth compounds with the same unit cells, all of which match the first decomposition product of the Fe-rich compositions, and, as such, the phase is likely $(Ba,Sr)_8(Fe,Co)_4O_{15}$.

BSF begins to decompose at 675 °C, with a second set of products beginning to form at 850 °C. The latter set of products includes SrO as a major phase, the other phases unidentified, and exists up to 1000 °C and upon cooling to RT. Adding some Co to form $Ba_{0.5}Sr_{0.5}Fe_{1-x}Co_xO_{3-\delta}$ with $x = 0.2$, results in the first decomposition at 650 °C, and the same phase evolution sequence as for BSF. Additional Co ($x = 0.4$), results in the same phase evolution sequence, however, the SrO becomes the primary phase detected as the second decomposition product and the Fe–Co alloy is clearly formed at high temperature. For the $Ba_{0.5}Sr_{0.5}Fe_{1-x}Co_xO_{3-\delta}$ ($x = 0.6$), initial decomposition occurs at 550 °C, again following the $x = 0.4$ phase evolution sequence and again increasing the amount of the Fe–Co alloy formed.

The first decomposition product changes at $x = 0.8$, as described above, and the end member BSC begins to decompose at 375 °C, forming $(Ba,Sr)_3(Co,Fe)O_5$ that decomposes by 450 °C to form SrO and the Co–Fe alloy. Further heating leads to reaction of the Ba to form (Ba,Sr)O with a significantly larger lattice constant than the initial SrO. On cooling to RT, the alloy and (Ba,Sr)O remain.

Additional experiments were conducted to understand the effects of phase decomposition on the microstructures of sintered pellets. Fig. 8 shows SEM micrographs of laboratory prepared $Ba_{0.5}Sr_{0.5}Fe_{0.2}Co_{0.8}O_{3-\delta}$ material, which was sintered at 1100 °C in air for 4 h before being heated under 4% hydrogen at 600 °C for varying lengths of time. As can be seen from the micrographs, even a short duration in the reducing atmosphere (10 min) causes significant damage to the BSCF microstructure as the decomposition products begin to form small discrete particles at the grain boundaries. Although the *in situ* XRD data show that BSCF can be recovered by heating in air, the micrographs demonstrate that microstructure is destroyed. Fig. 8(e) shows the microstructure after reheating in air (2 h at 600 °C) that is irreversibly destroyed. This demonstrates the importance of the phase stability of the fuel cell components to a wide range of atmospheric conditions, since although the desired phase may be recovered by changing the atmosphere, the microstructural damage caused by decomposition is irreversible and may result in failure of the device.

To investigate the effects of synthetic route/microstructure on the phase stability, a commercially available powder of significantly smaller particle size was also studied. Fig. 9 shows an SEM micrograph of the as-received commercial BSCF powder. The particles of the commercial powder are more irregularly shaped than the laboratory prepared particles and the particle size distribution is broad, ranging from a few tens of nanometers to a few microns.
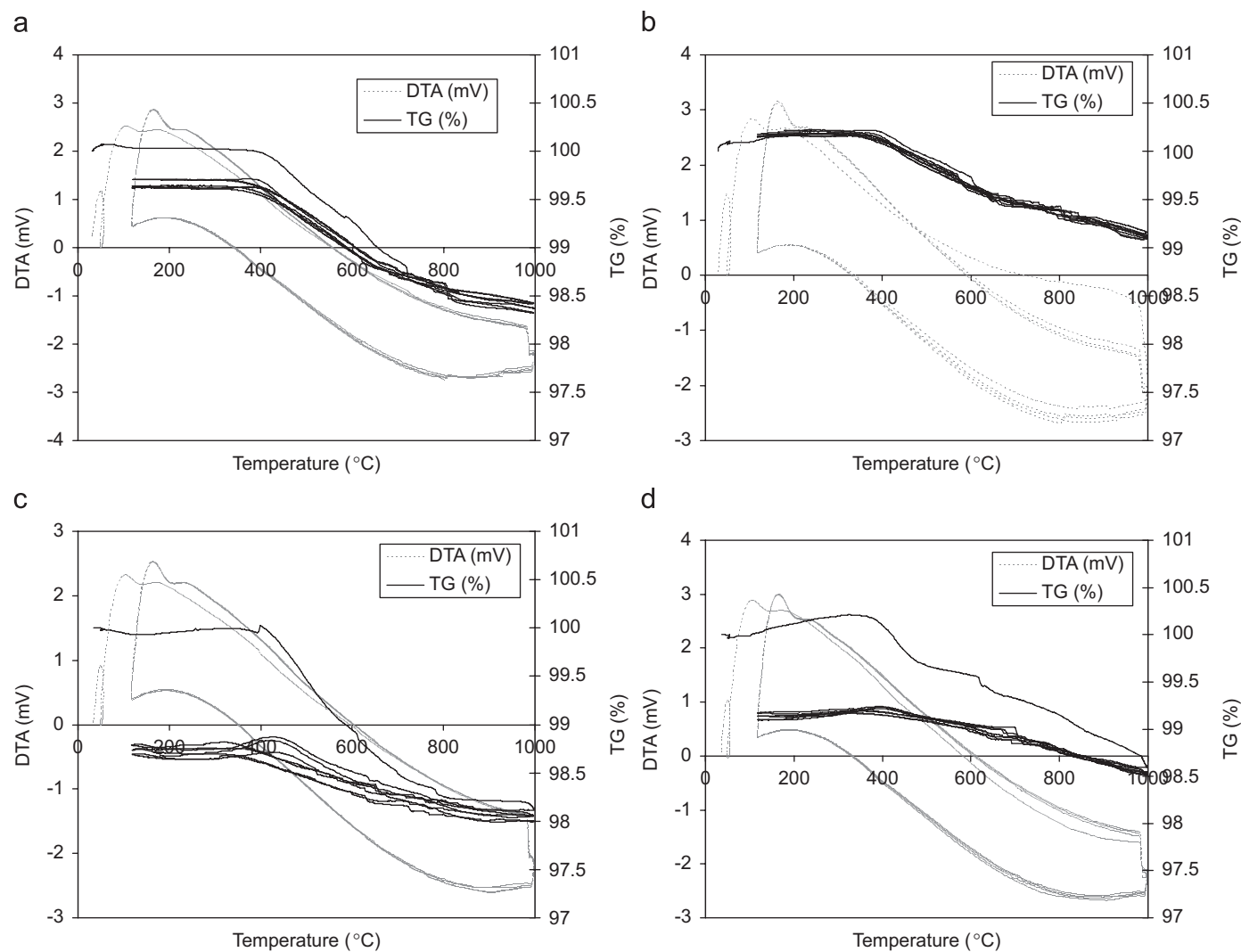
a

b

c

d

Fig. 6. TG/DTA data for laboratory prepared $Ba_{0.5}Sr_{0.5}Fe_{1-x}Co_xO_{3-\delta}$: (a) $x = 0.2$, air; (b) $x = 0.8$, air; (c) $x = 0.2$, 6×10^{-4} atm pO_2; and (d) $x = 0.8$, 6×10^{-4} atm pO_2.

Table 3
Initial weight loss together with gains and losses through thermal cycling in air and 6×10^{-4} atm pO_2 for $Ba_{0.5}Sr_{0.5}Fe_{1-x}Co_xO_{3-\delta}$

x	Atmosphere	Initial weight loss (%)	Weight gain on cooling (%)	Temperature of max weight (°C)
0.2	Air	1.6	1.2	398
0.4	Air	1.6	1.2	385
0.6	Air	1.4	1.0	390
0.8	Air	0.8	1.0	390
0.8 (commercial)	Air	6.6	1.1	275
0.2	6×10^{-4} atm pO_2	2.0	0.7	420
0.4	6×10^{-4} atm pO_2	1.5	0.6	401
0.6	6×10^{-4} atm pO_2	1.7	0.5	430
0.8	6×10^{-4} atm pO_2	1.5	0.5	413
0.8 (commercial)	6×10^{-4} atm pO_2	6.3	0.7	461

Fig. 10 shows X-ray diffraction data for the commercial BSCF powder heated to 1000 °C. For samples heated in 10^{-5} atm pO_2 (Fig. 10a) and 10^{-4} atm pO_2 (data not shown), the diffraction data was similar to that observed for the laboratory-prepared sample of the same composi-

tion in that the cubic pervoskite structure was retained upon heating 1000 °C. For samples heated in $10^{-3} < pO_2 <$ air, the formation of a secondary crystalline phase at ~675 °C was observed. The diffraction pattern of the phase matched the powder diffraction file entry for
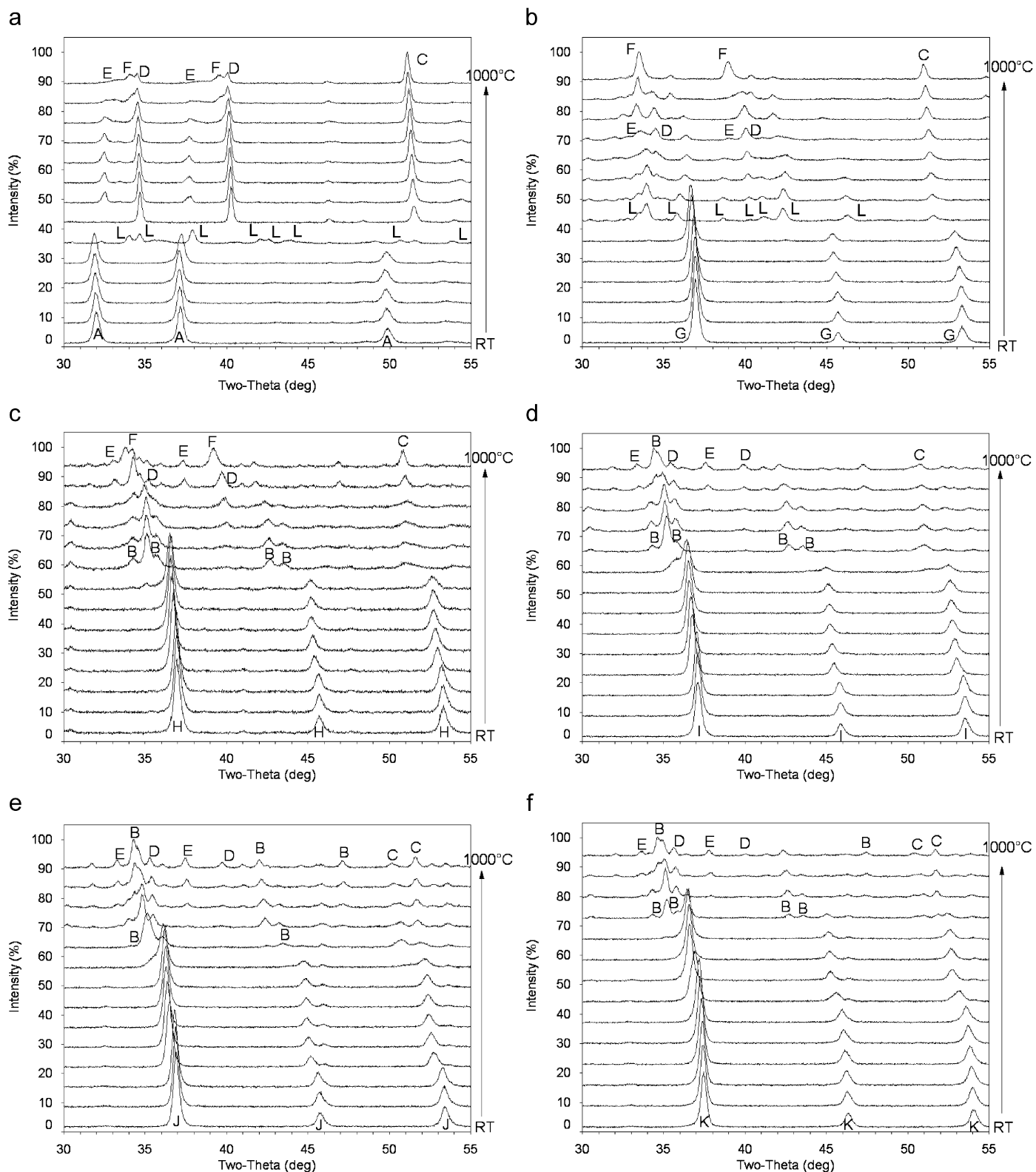
Fig. 7. *In situ* X-ray diffraction data for $Ba_{0.5}Sr_{0.5}Fe_{1-x}Co_xO_{3-\delta}$ heated in 4% H_2 in N_2. (a) $x = 1$, (b) $x = 0.8$, (c) $x = 0.6$, (d) $x = 0.4$, (e) $x = 0.2$, and (f) $x = 0$. Spectra are shown at 75 °C intervals for clarity. A = BSC, B = $(Ba,Sr)_8(Fe, Co)_4O_{15}$, C = (Fe,Co) alloy, D = SrO, E = BaO, F = $(Ba,Sr)O$, G = $Ba_{0.5}Sr_{0.5}Fe_{0.2}Co_{0.8}O_{3-\delta}$, H = $Ba_{0.5}Sr_{0.5}Fe_{0.4}Co_{0.6}O_{3-\delta}$, I = $Ba_{0.5}Sr_{0.5}Fe_{0.6}Co_{0.4}O_{3-\delta}$, J = $Ba_{0.5}Sr_{0.5}Fe_{0.8}Co_{0.2}O_{3-\delta}$, K = BSF, L = $(Ba,Sr)_3(Co,Fe)O_5$.

$Sr_6Co_5O_{15}$, PDF #086–0614. Considering the overall composition of the sample and the size of the cations involved, it is likely that the phase is a solid solution,

expressed as $(Sr,Ba)_6(Co,Fe)_5O_{15}$. With further heating to above 825 °C, the disappearance of the secondary phase is accompanied by an increase in the intensity of the BSCF
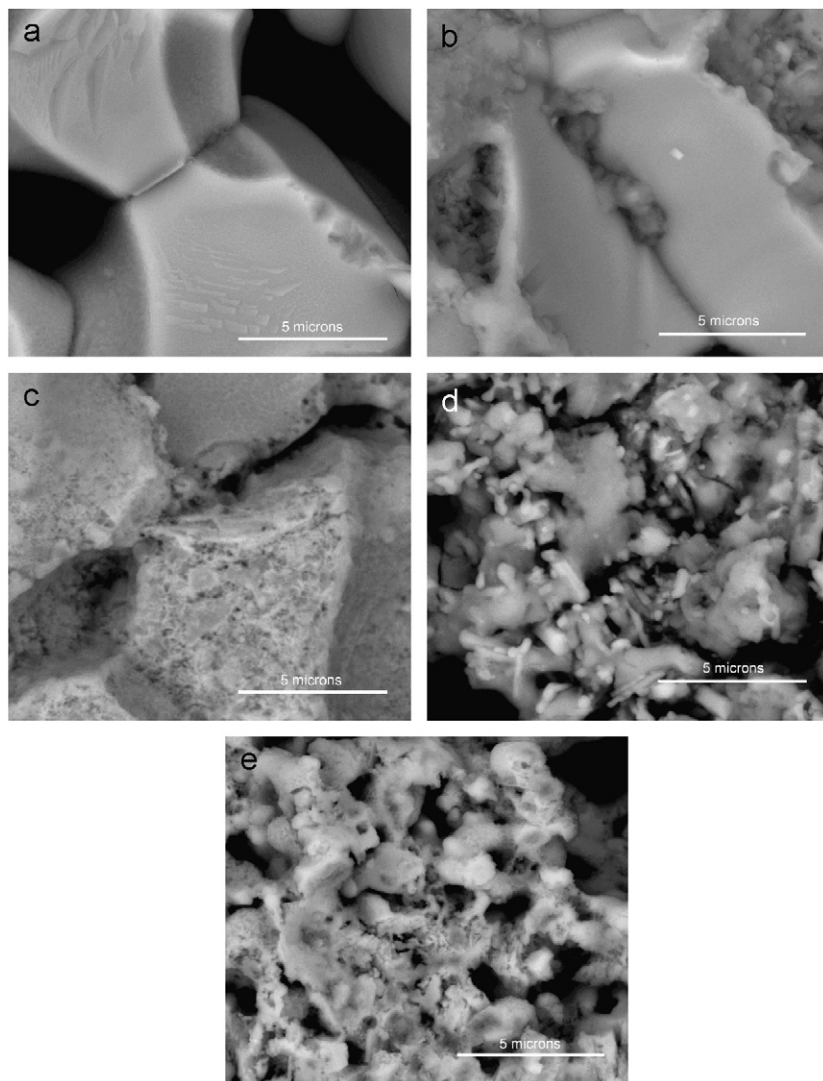
Fig. 8. SEM micrographs of laboratory prepared $Ba_{0.5}Sr_{0.5}Fe_{0.2}Co_{0.8}O_{3-\delta}$ powder, sintered in air at 1100 °C for 4 h then heated in 4% hydrogen in nitrogen at 600 °C, and then reheated in air at 600 °C. (a) As sintered powder; (b) 10 min 4% H_2; (c) 10 min 4% H_2 (600 °C), then 2 h air (600 °C); (d) 40 min 4% H_2; (e) 40 min 4% H_2 (600 °C), then 2 h air (600 °C).
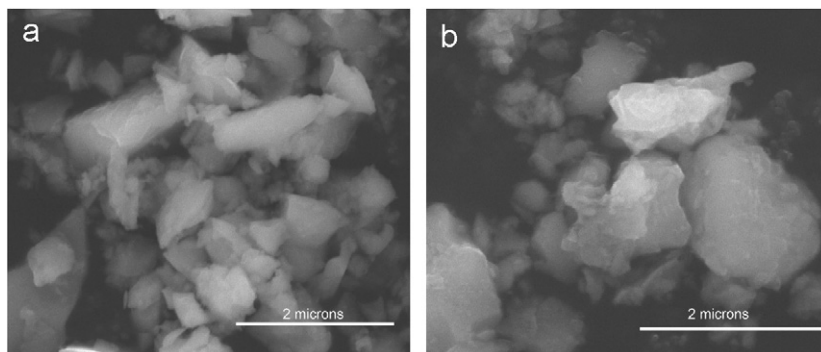

Fig. 9. SEM micrographs of commercial $Ba_{0.5}Sr_{0.5}Fe_{0.2}Co_{0.8}O_{3-\delta}$ showing the wide particle size distribution and irregular particle morphology.

peaks suggesting that the materials from the second phase are incorporated into the BSCF lattice. The secondary phase did not reappear upon cooling.

Fig. 11 shows the TGA of the commercial BSCF sample in air and 6×10^{-4} atm pO_2. Upon the first heating to 1000 °C, the samples exhibited 6–7% weight loss, which is
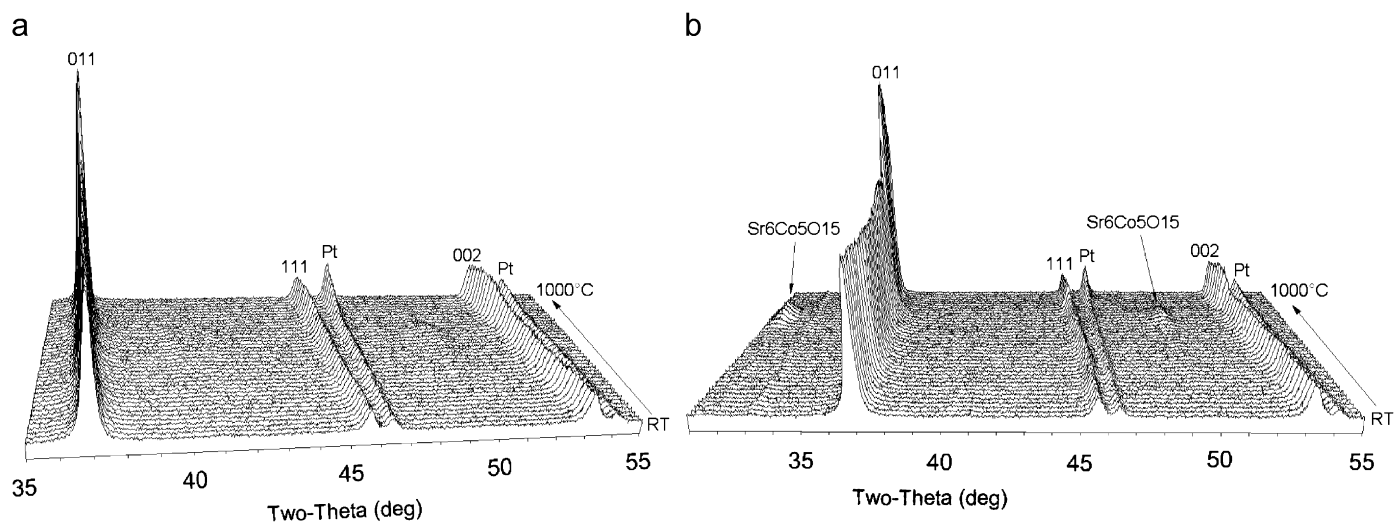
Fig. 10. *In situ* X-ray diffraction data for commercial $Ba_{0.5}Sr_{0.5}Fe_{0.2}Co_{0.8}O_{3-\delta}$ heated in varying partial pressures of oxygen: (a) 10^{-5} atm pO_2 demonstrating phase stability and (b) 10^{-2} atm pO_2 demonstrating the crystallization of a secondary phase. X-ray patterns are shown with temperature increments of 25 °C.
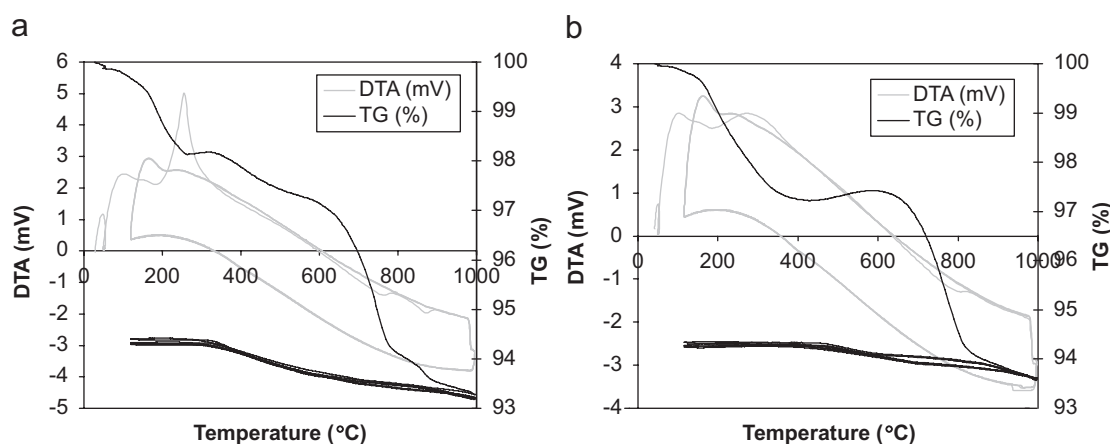

Fig. 11. TG/DTA curves for commercial $Ba_{0.5}Sr_{0.5}Fe_{0.2}Co_{0.8}O_{3-\delta}$ in (a) air and (b) 6×10^{-4} atm pO_2.

significantly higher than the 0.8–2% observed in the laboratory prepared powders. During the first heating cycle, an exothermic peak at ~250 °C was noted in the DTA curves of the commercially prepared samples, but not in the DTA curves of the laboratory-prepared powders. We speculate that the peak results from the combustion of residual organic materials in the commercial powder. Also noted in the DTA curves of the commercial samples is a small endothermic peak near 675–800 °C, which is presumably related to the formation of the secondary phase noted in the *in situ* X-ray diffraction data. After the initial ramp to 1000 °C, the TGA patterns of the commercial powders under air and reduced pO_2 are reproducible upon thermal cycling, and no significant peaks are noted in the DTA curves. However, hysteresis is observed in the heating and cooling curves of the sample tested in 6×10^{-4} atm pO_2. This is assumed to be the result of the broad particle size distribution, in which small

particles can equilibrate with the atmosphere faster than the larger particles.

Fig. 12 shows the X-ray diffraction patterns for the commercial $Ba_{0.5}Sr_{0.5}Fe_{0.2}Co_{0.8}O_{3-\delta}$ as it is heated in 4% H_2 in N_2. The BSCF is stable up to a temperature of 300 °C, however, at 325 °C the BSCF starts to decompose rapidly to form the Ba_3FeO_5-type phase, which is expected to be a solid solution expressed as $(Ba,Sr)_3(Co,Fe)O_5$. By 375 °C the BSCF has been almost completely eliminated and the decomposition products have fully formed. At 550 and 725 °C, further decomposition reactions occur, forming unidentified intermediates. The final decomposition step begins at 900 °C to form $Ba_{0.5}Sr_{0.5}O$ and a Co–Fe alloy. All of the reaction products remain on cooling to RT. Comparison of the laboratory prepared $Ba_{0.5}Sr_{0.5}Fe_{0.2}Co_{0.8}O_{3-\delta}$ with the commercial product showed clear similarities. While the initial decomposition temperatures differ (325 °C vs. 425 °C for the laboratory product), the

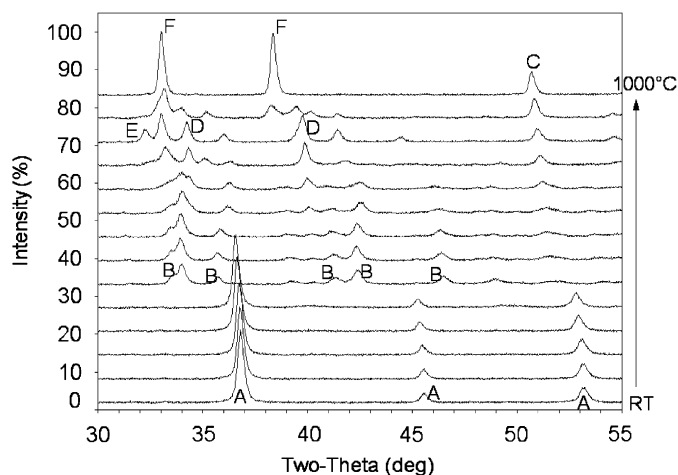Fig. 12. *In situ* X-ray diffraction patterns of commercial $Ba_{0.5}Sr_{0.5}Fe_{0.2}Co_{0.8}O_{3-\delta}$ heated in 4% H_2. X-ray patterns are shown with temperature increments of 75 °C. $A = Ba_{0.5}Sr_{0.5}Fe_{0.2}Co_{0.8}O_{3-\delta}$, $B = (Ba,Sr)_3(Co,Fe)O_5$, $C = (Fe, Co)$ alloy, $D = SrO$, $E = BaO$, $F = (Ba,Sr)O$.

decomposition products appear to be largely the same for both powders. After the initial decomposition, the remaining reactions for the two $Ba_{0.5}Sr_{0.5}Fe_{0.2}Co_{0.8}O_{3-\delta}$ powders become identical, both in terms of decomposition temperatures and products (see Fig. 7).

4. Conclusions

The phase stability of BSCF $Ba_{0.5}Sr_{0.5}Fe_{1-x}Co_xO_{3-\delta}$ ($x = 0$–1) has been investigated using high-temperature X-ray diffraction and TG/DTA. All BSCF compositions and the end member BSF were stable down to 10^{-5} atm pO_2 to 1000 °C. The other end member, BSC, undergoes a phase transition at 10^{-5} atm pO_2 at ~825 °C to a cubic perovskite. The phase transition is irreversible on cooling, yielding a defect perovskite at RT with $a = 3.9892(3)$ Å and unit cell volume = 63.48(2) Å^3. As for other transition-metal perovskites, BSCF displays significant oxygen nonstoichiometry that is a strong function of temperature and oxygen partial pressure. The oxygen transport rates are fast enough to be cycled at 10 K/min without hysteresis for powder samples.

The temperature range of stability of BSCF under reducing conditions is a strong function of the Co/Fe ratio. Initial decomposition occurs under 4% H_2 from 375 to 675 °C, depending on the Co/Fe ratio, with higher Fe content improving the stability. Although the phase decomposition under reducing atmosphere is fully reversible on reheating in air, the microstructures of dense sintered bodies is irreversibly destroyed. Preparation method also strongly influences the reduction behavior of

the powder in terms of non-stoichiometry, which ultimately will affect its electrical properties at high temperature since they are dependent upon the presence of oxygen ion vacancies in the lattice. This may well be an important factor in determining the final choice of material for use in a fuel cell stack.

Acknowledgment

References

[1] Z. Shao, W. Yang, Y. Cong, H. Dong, J. Tong, G. Xiong, J. Membr. Sci. 172 (2000) 177–188.
[2] Z.P. Shao, H. Dong, G.X. Xiong, Y. Cong, W.S. Yang, J. Membr. Sci. 183 (2001) 181–192.
[3] Z. Shao, S.M. Haile, Nature 431 (2004) 170–173.
[4] Z. Duan, M. Yang, A. Yan, Z. Hou, Y. Dong, Y. Chong, M. Cheng, W. Yang, J. Power Sources 160 (2006) 57–64.
[5] Q. Zhu, T. Jin, Y. Wang, Solid State Ion. 177 (2006) 1199–1204.
[6] Q.L. Liu, K.A. Khor, S.H. Chan, J. Power Sources 161 (2006) 123–128.
[7] J. Pena-Martinez, D. Marrero-Lopez, J.C. Ruiz-Morales, B.E. Buergler, P. Nunez, L.J. Gaukler, Solid State Ion. 177 (2006) 2143–2147.
[8] M.D. Mat, X. Liu, Z. Zhu, B. Zhu, Int. J. Hydrogen Energy 32 (2007) 796–801.
[9] S. Lee, Y. Lim, E.A. Lee, H.J. Hwang, J.W. Moon, J. Power Sources 157 (2006) 848–854.
[10] B. Liu, Y. Zhang, J. Alloys Compd., in press, available online December 26, 2007.
[11] A. Subramania, T. Saradha, S. Muzhumathi, J. Power Sources 165 (2) (2007) 728–732.
[12] S. Li, Z. Lu, N. Ai, K. Chen, W. Su, J. Power Sources 165 (2007) 97–101.
[13] S. Li, Z. Lu, B. Wei, X. Huang, J. Miao, Z. Liu, W. Su, J. Alloys Compd. 448 (1–2) (2008) 116–121.
[14] S. Li, Z. Lu, B. Wei, X. Huang, J. Miao, G. Cao, R. Zhu, W. Su, J. Alloys Compd. 426 (2006) 408–414.
[15] W. Zhou, Z. Shao, R. Ran, P. Zeng, H. Gu, W. Jin, N. Xu, J. Power Sources 168 (2007) 330–337.
[16] Y. Wang, S. Wang, Z. Wang, T. Wen, Z. Wen, J. Alloys Compd. 428 (2007) 286–289.
[17] A. Yan, M. Cheng, Y. Dong, W. Yang, V. Maragou, S. Song, P. Tsiakaras, Appl. Catal. B: Environ. 66 (2006) 64–71.
[18] S. McIntosh, J.F. Vente, W.G. Haije, D.H.A. Blank, H.J.M. Bouwmeester, Solid State Ion. 177 (2006) 1737–1742.
[19] S. McIntosh, J.F. Vente, W.G. Haije, D.H.A. Blank, H.J.M. Bouwmeester, Chem. Mater. 18 (2006) 2187–2193.
[20] Y.H. Lim, J. Lee, J.S. Yoon, C.E. Kim, H.J. Hwang, J. Power Sources 171 (1) (2007) 79–85.
[21] Z. Chen, R. Ran, W. Zhou, Z. Shao, S. Liu, Electrochim. Acta. 52 (25) (2007) 7345–7351.
[22] S.T. Misture, Measure. Sci. Tech. 14 (2003) 1091–1098.
[23] J. Ovenstone, J.S. White, S.T. Misture, J. Power Sources, submitted for publication.